

A Macroquantification Approach for Region-of-Interest Assessment in Emission Tomography

Fayçal Ben Bouallègue, PhD

Abstract: In this article, we propose a quantification methodology for estimating the statistical parameters of the activity inside regions of interest (ROIs). Macroquantification implies a rearrangement of the emission projection data into macroprojections and a redefinition of the system matrix based either on an image reconstruction involving iterative ROI-wise regularization or on an ROI uniformity assumption. The technique allows a very fast computation of the ROI activities and covariance matrix in the least squares sense using a low-dimensional model of the tomographic problem. The macroquantification approach is evaluated through Monte Carlo simulations using a numerical thorax phantom, without taking into account the measurement artifacts and assuming a perfect a priori ROI definition. Various tumor ROI configurations and count rates are considered to reflect clinical situations. The results show that our technique yields low-bias ROI estimations that turn out to be more accurate than classical estimates relying on pixel summation. Macroquantification also provides an approximation for the ROI variance that describes the effective variance obtained through the simulations fairly well. The technique is then validated using single photon emission computed tomography (SPECT) data from a physical phantom composed of cylinders filled with different ^{99m}Tc concentrations for the task of ROI comparison. Here again, the study shows excellent agreement between the measured and predicted values of the ROI variance resulting in efficient estimations of ROI ratios and highly accurate ROI comparisons. In its simplest formulation, macroquantification has a short computation time, making it an ideal technique for quantitative ROI assessment that is compatible with a wide range of routine clinical applications.

Key Words: emission tomography, region-of-interest quantification, variance estimation

(*J Comput Assist Tomogr* 2013;37: 770–782)

Quantitative interpretation in emission tomography requires evaluating the uncertainty (ie, the variance) of the reconstructed images. This is particularly true when one has to quantify or to compare the total activity inside one or several regions of interest (ROIs) having potential clinical interest. The problem of estimating image variance in emission tomography has been extensively studied. Analytical and numerical approximations have been proposed, many of them focusing on a particular reconstruction algorithm. Both filtered backprojection and maximum-likelihood (ML) algorithms have been studied since the late 70s in emission tomography, and many approximations have been proposed to describe the propagation of the uncertainty from the recorded data to the reconstructed images.^{1–21} In 1996, Fessler drew a theoretical framework for characterizing the variance of implicitly defined estimators that yields an

approximation for the particular case of emission tomography.²² Original methods based on bootstrapping techniques^{23,24} or intervalist prediction^{25,26} have also been proposed. The computation of the whole reconstructed image covariance matrix, however, remains a fastidious task because of the huge dimensions (typically of $O[10^4 \times 10^4]$) of the system matrix in classical tomographic configuration. The difficult handling of the numerical errors (resulting from the ill conditioning of the system matrix) and its heavy computational complexity make this task unsuitable for clinical routine. In addition, routine image interpretation requires ROI assessment rather than pixelwise variance estimation. After the previous attempts to design ROI-based techniques in emission tomography,^{27–31} the aim of the present study was to describe a macroquantification approach for the computation of predefined ROIs activity and variance. The method allows a very fast computation of the ROI activities and covariance matrix in the least squares sense using a low-dimensional model of the tomographic problem specially dedicated to ROI study. When the ROI boundaries are accurately defined, it also provides ROI estimates that are significantly less biased than classical estimates based on pixel summation. We show that, from a dimensional point of view, the variance estimates provided by our method fit perfectly with the classical approximate formulations proposed by Huesman¹ and Budinger et al.² The macroquantification is first evaluated through Monte Carlo simulations using a numerical thorax phantom with tumorlike ROIs for the estimation of the ROI statistical parameters. The technique is then validated using a physical phantom SPECT acquisition for the task of ROI comparison.

MATERIALS AND METHODS

Classical ROI Quantification

Let $\bar{\theta} \in \mathbb{R}^N$ be an activity distribution defined on a Cartesian grid, with N as the number of pixels sampling the field of view of the acquisition device. Let $\bar{\mathbf{p}} \in \mathbb{R}^{\text{BD}}$ be the exact projections of $\bar{\theta}$, where BD is the total number of recorded projections (with D as the number of projection angles and B as the number of bins per projection angle). Let $\Lambda \in \mathbb{R}^{\text{BD} \times N}$ be the radon operator (or system matrix) such that $\bar{\mathbf{p}} = \Lambda \bar{\theta}$. The system matrix component Λ_{ij} gives the probability for a photon emitted from pixel j to be recorded into projection i . Ideally, the system matrix should perfectly model the emission/detection process, including adverse effects such as autoattenuation, Compton scattering, and detector response function. The actual recorded projections $\mathbf{p} \in \mathbb{R}^{\text{BD}}$ are affected by Poisson noise, and it is commonly accepted that $\text{Var}(\mathbf{p}) \approx \text{Diag}(\mathbf{p})$ represents a good approximation of the data variance. Tomographic reconstruction intends to produce an estimator $\hat{\theta} \in \mathbb{R}^N$ of the original image $\bar{\theta}$ starting from the recorded projections \mathbf{p} . Most of modern reconstruction algorithms are statistical in the sense that they build up this estimator on the basis of the conditional probability of

From the Department of Biophysics and Nuclear Medicine, Montpellier Medical University, Montpellier, France.

Received for publication April 5, 2013; accepted May 18, 2013.

Reprints: Fayçal Ben Bouallègue, PhD, Department of Biophysics and Nuclear Medicine, Montpellier Medical University, 34295 Montpellier, France (e-mail: faybenb@hotmail.com).

The author certifies that there is no conflict of interest with any financial organization regarding the material discussed in the article.

Copyright © 2013 by Lippincott Williams & Wilkins

the sought-after image knowing the projections. This probability is usually called the posterior $L(\theta, \mathbf{p})$ and can be written using the Baye theorem:

$$L(\theta, \mathbf{p}) = \wp(\theta|\mathbf{p}) = \wp \frac{\wp(\mathbf{p}|\theta) \wp(\theta)}{\wp(\mathbf{p})} \quad (1)$$

where the likelihood $\wp(\mathbf{p}|\theta)$ is such that

$$\wp(\mathbf{p}|\theta) = \prod_i \frac{e^{-\Lambda\theta_i} (\Lambda\theta_i)^{p_i}}{p_i!} \quad (2)$$

The most straightforward way to design an estimator (which is also one of the most commonly used in practice) consists in searching the image that maximizes the log-posterior:

$$\hat{\theta} = \underset{\theta \in \mathbb{R}^N}{\operatorname{argmax}} [\log (L(\theta, \mathbf{p}))] \quad (3)$$

When one considers that no prior information is available concerning the reconstructed object, the probability $\wp(\theta)$ is set to constant and equation (3) defines the ML estimator.^{32,34} No explicit formulation of this estimator can be derived, and its computation is achieved using the iterative expectation-maximization algorithm (MLEM). MLEM is known to provide a low-bias estimator (at least asymptotically at high count rates) for which the Cramér-Rao bound (CRB) gives a lower limit of the covariance:

$$\operatorname{Cov}(\hat{\theta}) \geq \mathbf{F}^{-1} \quad (4)$$

with \mathbf{F} as the Fisher information matrix:

$$\mathbf{F} = E \left(-\frac{\partial^2}{\partial \theta^2} \log (L(\theta, \mathbf{p})) \right) = \Lambda^T \mathbf{C}^{-1} \Lambda \quad (5)$$

where \mathbf{C} stands for the covariance matrix of the recorded data:

$$\mathbf{C} = \operatorname{Cov}(\mathbf{p}) = \operatorname{Diag}(\bar{\mathbf{p}}) \approx \operatorname{Diag}(\mathbf{p}) \quad (6)$$

However, the ML estimator is known to amplify the acquisition noise through the reconstruction process, especially at low-count rates.³⁵ Its covariance is thus highly dependent on the number of iterations after which the iterative algorithm is stopped and the CRB can no longer provide an accurate variance prediction. In addition, there exists no consensual stopping criterion allowing an optimal management of the noise-resolution tradeoff.

When dealing with ROI activities, the following notations will be used. K will denote the number of ROIs in the studied object (usually $K = 2$, ie, 1 ROI plus the background). $\Psi \in \mathbb{R}^K$ will denote the true activity inside the ROIs and $\hat{\Psi} \in \mathbb{R}^K$ will stand for the estimator of the ROI activities. Defining $\kappa \in \{0,1\}^{K \times N}$, the characteristic function of the

ROIs is $\kappa_{kj} = 1$ if pixel j is inside ROI k ; $\kappa_{kj} = 0$ otherwise, one can write the following:

$$\bar{\Psi} = \kappa \bar{\theta} \quad (7)$$

The ROI estimator is usually obtained after the reconstruction process by simply summing the pixel values of the image esti-

mator $\hat{\theta}$ inside the studied ROIs:

$$\hat{\Psi} = \kappa \hat{\theta} \quad (8)$$

One may then use the CRB to compute a lower limit of the ROI estimator covariance using the following:

$$\operatorname{Cov}(\hat{\Psi}) \geq \kappa \operatorname{Cov}(\hat{\theta}) \kappa^T \quad (9)$$

However, some critical points have to be discussed regarding this classical ROI quantification technique. When nonregularized reconstruction algorithms are exploited to produce the image estimator, the bias affecting the ROI estimate is controlled by letting the algorithm reach convergence through a sufficient number of iterations. Yet, the ROI variance remains hardly foreseeable using the CRB because the noise affecting the image estimate is strongly related to the total number of iterations (this appears clearly in our Results section; Figs. 5 and 6). When regularized algorithms are used, the ROI variance amplification can be effectively subdued if correct smoothing parameters are chosen but at the price of an increase in the systematic bias. Lastly, from a practical point of view, the computation of the image covariance matrix using the CRB remains a hazardous task because of the huge dimensions and ill conditioning of the system matrix to be inverted. These last considerations justify our attempt to develop an innovative formulation of the tomographic problem in a macroscopic perspective, as presented in the following section.

Macroquantification

Classical tomographic reconstruction addresses the task of building an image using its projection data. The image is built over a Cartesian kernel constituted of pixels representing basic image elements inside which the activity may be considered as uniform. In the particular case of emission tomography, the difficulty follows from the uneasy handling of a large system matrix Λ linking a large number of pixel values θ with a large number of highly noisy projections \mathbf{p} . The huge dimensions of the linear system combined with the presence of a significant amount of noise impede a simple and efficient computation of the image estimator as well as its variance. The macroquantification approach intends to simplify the formulation of the problem by means of a model downsampling dedicated to ROI quantification. The studied object will be divided into K ROIs ($R_k, k = 0 \dots K - 1$) indexed with the letter k , one being the background (ROI R_0) and the following (R_1, R_2, \dots) being the studied ROIs themselves. These K ROIs will be considered as the basic components of the reconstructed image, acting as the pixels in classical tomography. As previously mentioned, the ROI estimator will be denoted as $\hat{\Psi} \in \mathbb{R}^K$. To further reduce the system complexity, the projection data will also be

aggregated to create macroprojections denoted as \mathbf{P} . For each projection \mathbf{p}_i , let us note

$$\gamma_i = \{R_{i,1}, \dots, R_{i,m}\} : \forall k, R_k \in \gamma_i \text{ if } \{\exists j \in R_k \mid \Lambda_{ij} > 0\} \quad (10)$$

as the set of ROIs that contain at least 1 pixel projecting onto \mathbf{p}_i . Let

$$\Gamma = \{\gamma_1, \dots, \gamma_T\} : \forall (t_1, t_2) t_1 \neq t_2, \gamma_{t_1} \neq \gamma_{t_2} ; \forall i, \{\exists t, 1 \leq t \leq T \mid \gamma_i = \gamma_t\} \quad (11)$$

be the complete set of T distinct values of γ .

The projections are then aggregated into T macroprojections $\mathbf{P} \in \mathbb{R}^T$:

$$\mathbf{P}_t = \sum_{i \mid \gamma_i = \Gamma_t} \mathbf{p}_i \quad (12)$$

Figure 1 illustrates the situation for $K = 3$ ROIs. The aggregation process produces $T = 4$ macroprojections using $\Gamma = \{\{R_0\}, \{R_0, R_1\}, \{R_0, R_2\}, \{R_0, R_1, R_2\}\}$: \mathbf{P}_1 sums all the projections that only intersect the background; \mathbf{P}_2 , those intersecting both R_0 and R_1 ; \mathbf{P}_3 , those intersecting both R_0 and R_2 ; and \mathbf{P}_4 , those intersecting the 3 ROIs. Because R_1 and R_2 are located inside R_0 , there is trivially no projection intersecting R_1 and/or R_2 without intersecting R_0 .

From the macroscopic point of view, the ROI values Ψ are linked with the macroprojections \mathbf{P} through a linear system $\mathbf{P} = \mathbf{M}\Psi$. The macroprojector $\mathbf{M} \in \mathbb{R}^{T \times K}$ is such that its element M_{tk} gives the probability for a photon emitted from ROI k to be detected into macroprojection t . For a given object θ , this probability depends on the activity distribution inside the ROIs following:

$$M_{tk} = \frac{\sum_{j \in R_k} \sum_{i \mid \gamma_i = \Gamma_t} \Lambda_{ij} \bar{\theta}_j}{\sum_{j \in R_k} \sum_i \Lambda_{ij} \bar{\theta}_j} \quad (13)$$

The Fisher information matrix \mathbf{F} related to the macroscopic problem $\mathbf{P} = \mathbf{M}\Psi$ is as follows:

$$\mathbf{F} = \mathbf{M}^T \text{Cov}^{-1}(\mathbf{P}) \mathbf{M} \approx \mathbf{M}^T \text{Diag}^{-1}(\mathbf{P}) \mathbf{M} \quad (14)$$

Because the macroprojections naturally gather a high number of events, the estimator of the ROI activities can be computed in the least squares sense using the following:

$$\hat{\Psi} = \mathbf{F}^{-1} \mathbf{M}^T \text{Diag}^{-1}(\mathbf{P}) \mathbf{P} \quad (15)$$

and the ROI estimator variance may hence be approximated using the following:

$$\text{Cov}(\hat{\Psi}) = \mathbf{F}^{-1} \approx [\mathbf{M}^T \text{Diag}^{-1}(\mathbf{P}) \mathbf{M}]^{-1} \quad (16)$$

Compared with the standard approach, the macroscopic approach (equations [15] and [16]) offers ROI quantification expressions that are easily computable by inverting very low dimension matrices. The produced ROI estimator is naturally unbiased and its variance is readily predictable. We show in Dimensional Study section in the following paragraphs that, from a dimensional point of view, equation (16) produces estimates of the ROI variance that are in agreement with the classical approximations of Huesman¹ and Budinger et al.²

Computation of the Macroprojector

In the last section, we proposed a macroscopic approach to drastically reduce the system dimensions dedicated to ROI assessment. This reduction relies on a model downsampling from pixels to ROIs and from projections to macroprojections. The aggregation process, which affects both the data and the unknowns of the problem, inevitably induces a loss of information. The missing information is synthesized into the macroprojector, which is the keystone of the macroscopic model. For a given studied object, the components of the macroprojector depend on the exact activity distribution inside the object, as defined through equation (13). In practice, the original object remains unknown and the macroprojector has to be modelled starting from the data of the problem, that is, the recorded noisy projections. The computation of the macroprojector can be performed using equation (13), where the exact activity distribution θ is replaced with an image estimate $\hat{\theta}$:

$$M_{tk} = \frac{\sum_{j \in R_k} \sum_{i \mid \gamma_i = \Gamma_t} \Lambda_{ij} \hat{\theta}_j}{\sum_{j \in R_k} \sum_i \Lambda_{ij} \hat{\theta}_j} \quad (17)$$

This estimate has to fulfill certain requirements to ensure sufficient accuracy and robustness of the macroprojector (Fig. 2). First, this estimate has to be regularized so as to warrant the stability of the macroprojector in the presence of noise. However, if a global regularization or postfiltering of the object estimate

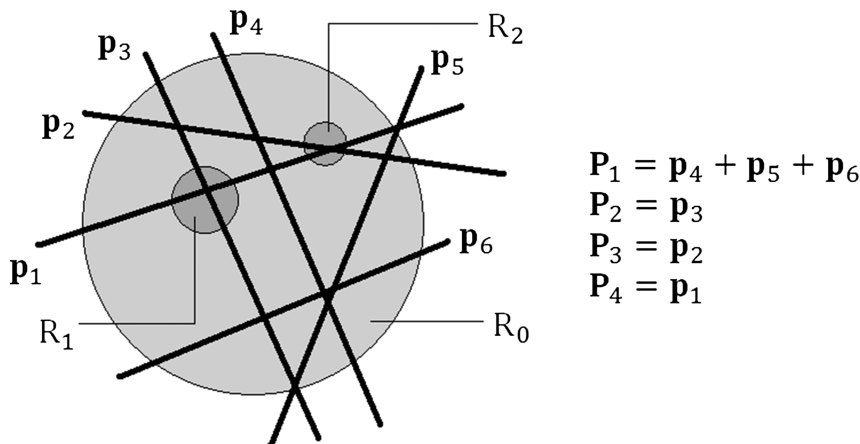


FIGURE 1. Aggregation of the projections into macroprojections in a 3-ROI configuration.

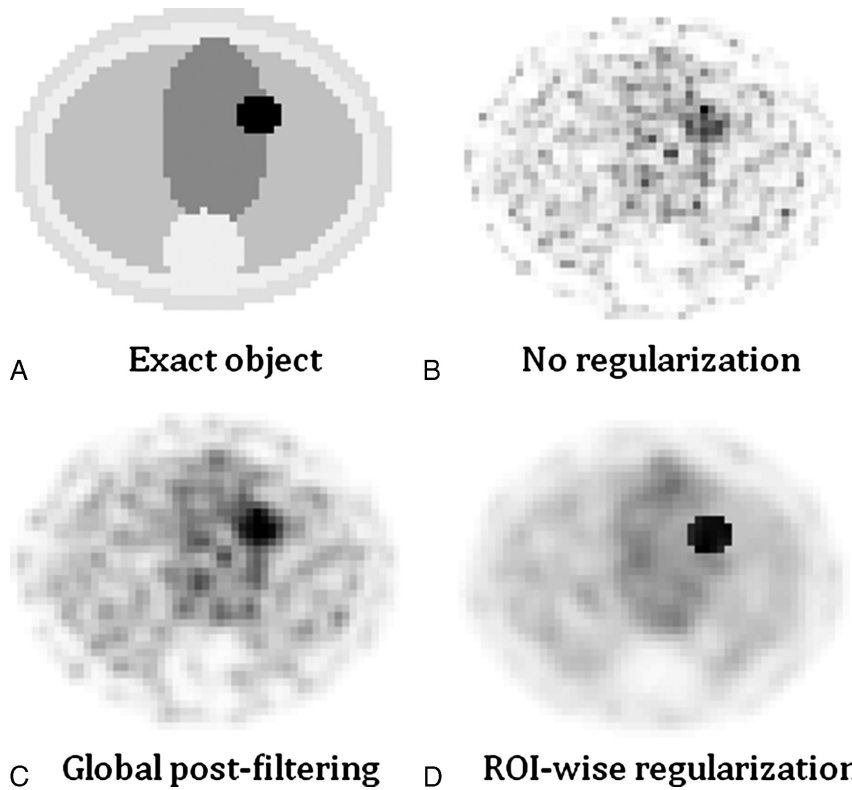


FIGURE 2. A, Exact object. B, MLEM of 100 iterations. C, MLEM of 100 iterations followed by gaussian postfiltering of FWHM 2 pixels. D, MLEM of 100 iterations with iterative ROI-wise gaussian filtering of FWHM 1 pixel.

is performed, the macroprojector will suffer from the resolution loss around the borders between the ROIs. One solution for the conjunct handling of both noise and resolution relies on an iterative ROI-wise regularization of the object estimate (similar reconstruction algorithms have already been proposed³⁵⁻³⁷). An MLEM scheme is used to reconstruct the image. In between each iteration step, a convolution of the current estimated activity is performed inside each ROI with a gaussian filter. Denoting $R(j)$ as the ROI containing pixel j , an iteration step is performed using the following:

•MLEM update:

$$\theta_j^{n+1/2} = \theta_j^n \frac{\sum_i \Lambda_{ij} \frac{p_i}{(\Lambda \theta^n)_i}}{\sum_i \Lambda_{ij}} \quad (18)$$

• ROI-wise smoothing:

$$\theta_j^{n+1} = \frac{\sum_{q \in R(j)} G_{j,s}(q) \theta_q^{n+1/2}}{\sum_{q \in R(j)} G_{j,s}(q)} \quad (19)$$

where $G_{j,s}$ stands for a gaussian kernel centered on pixel j with a standard deviation of s pixels. Using this reconstruction technique will allow the macroprojector to be accurate and robust with respect to the noise. To be fully efficient, this technique requires a good knowledge of the ROI boundaries so that the high-activity region can be precisely discriminated from the low-activity background. Because the coupling of SPECT and positron emission tomographic (PET) acquisition with computed

tomographic (CT) scanning has tended to generalize, the circumscription of the ROIs may often be performed with the help of the coregistered morphological information for an optimal computation of the macroprojector. When no morphological information is available, one has to exploit a prior image reconstruction for the definition of the ROIs. In the particular case where the defined ROIs are a priori known to have a uniform activity distribution, one will rely on the use of the uniform macroprojector U , which can be built naturally without preliminary image reconstruction:

$$U_{tk} = \frac{\sum_{j \in R_k} \sum_{i | \gamma_i = \Gamma_t} \Lambda_{ij}}{\sum_{j \in R_k} \sum_i \Lambda_{ij}} \quad (20)$$

Dimensional Study

In this section, we study the order of magnitude of the variance computed with equation (16). We assume that the recorded projections are $O(p)$. The image is reconstructed on a grid of dimensions $N \times N$. Let us consider a circular uniform ROI of diameter Δ pixels called R_A . A second ROI R_B is defined as a pixel inside R_A (Fig. 3). For each projection angle, the object projects onto $\Delta B/N$ bins. The total counts recorded are thus $O(p \times D \times \Delta B/N)$, with p as the order of magnitude of a single projection. From the fact that the total counts recorded in the projections must be recovered in the reconstructed image θ , one can infer that θ is $O(\frac{\text{total counts}}{\Delta^2}) = O(\frac{BDp}{N\Delta})$.

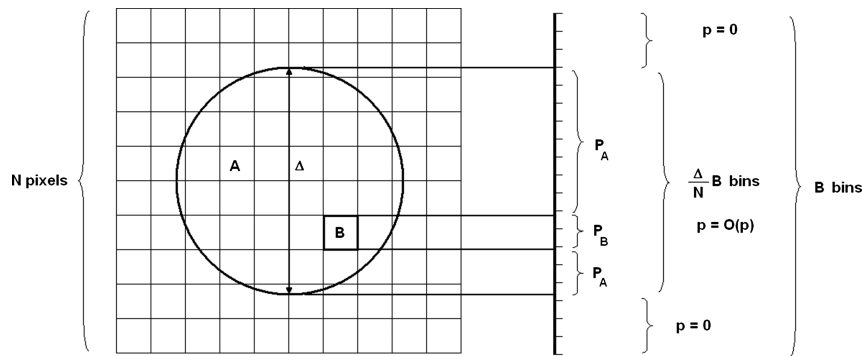


FIGURE 3. Case of 2 ROIs, one being a single pixel.

Concerning the mean of the global activity Ψ_A inside R_A , one has the following:

$$\Psi_A = O(\Delta^2 \theta) = O(\text{total counts}) = O\left(\frac{\Delta B D p}{N}\right) \quad (21)$$

As for the mean activity Ψ_B inside R_B , one has the following:

$$\Psi_B = O(\theta) = O\left(\frac{B D p}{N \Delta}\right) \quad (22)$$

One rearranges the projections into 2 macroprojections:

$$\bar{P}_A = O\left(\frac{\Delta B D p}{N}\right) ; \quad \bar{P}_B = O\left(\frac{B D p}{N}\right) \quad (23)$$

Noting that the coefficients of \mathbf{M} are $O(1)$ for the couples (R_A, \bar{P}_A) and (R_B, \bar{P}_B) and $O(0)$ for the couples (R_A, \bar{P}_B)

and (R_B, \bar{P}_A) , one computes the components of the 2×2 Fisher information matrix \mathbf{F} as follows:

$$\begin{aligned} \mathbf{F}_{AA} &= O\left(\frac{N}{\Delta B D p}\right) ; \quad \mathbf{F}_{BB} = O\left(\frac{N}{B D p}\right) ; \quad \mathbf{F}_{AB} \\ &= \mathbf{F}_{BA} = O(0) \end{aligned} \quad (24)$$

The matrix \mathbf{F} being approximately diagonal, the variance of the activities into R_A and R_B are given by the following:

$$\sigma_A^2 \approx \mathbf{F}_{AA}^{-1} = O\left(\frac{\Delta B D p}{N}\right) \quad (25)$$

$$\sigma_B^2 \approx \mathbf{F}_{BB}^{-1} = O\left(\frac{B D p}{N}\right) \quad (26)$$

Comparing equation (21) with equation (25), it follows that $\sigma_A^2 \approx \Psi_A$, which is in agreement with the Poisson law describing

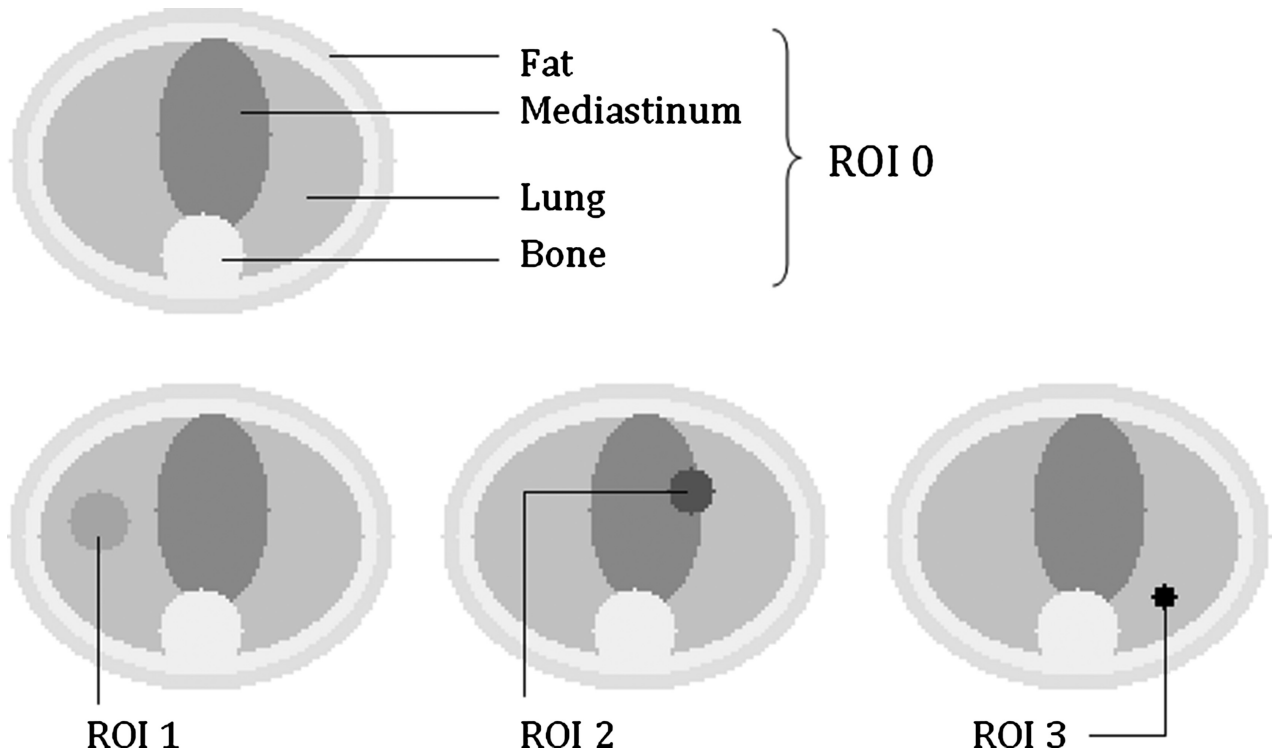


FIGURE 4. Top, The studied numerical phantom. Bottom, The 3 studied tumor ROI configurations.

TABLE 1. Composition of the Numerical Thorax Phantom

Tissue	Relative Uptake
Bone	1
Fat	2
Lung	4
Mediastinum	8

the distribution of radioactive measurement. From equations (22) and (26), one computes an estimate of the ratio σ_B/Ψ_B :

$$\frac{\sigma_B}{\Psi_B} \approx \frac{\sqrt{BDp}}{\sqrt{N}} \frac{N\Delta}{BDp} = \frac{\sqrt{p}}{p} \frac{1}{\sqrt{BD}} \Delta \sqrt{N} \quad (27)$$

which can be rewritten, provided that the object has roughly the dimensions of the field of view (ie, $\Delta \approx N$):

$$\frac{\sigma_B}{\Psi_B} \approx \frac{\sqrt{p}}{p} \frac{1}{\sqrt{BD}} \Delta^{3/2} \quad (28)$$

Equation (28) is strictly equivalent to Huesman's formula¹ (equation [15]), which states that the ratio between the standard deviation and the mean activity of a pixel into a circular ROI can be approximated by the ratio between the standard deviation and the mean of the recorded projections, times a multiplicative factor, this factor being the following: (the ratio between the size of the ROI and the size of the pixel) power 3/2 divided by the square root of the total number of projections. Denoting W as the number of pixels into ROI A ($W = O(\Delta^2)$), equation (27) can be rewritten as follows:

$$\begin{aligned} \frac{\sigma_B}{\Psi_B} &= \frac{1}{\sqrt{\Psi_B}} \frac{\sigma_B}{\sqrt{\Psi_B}} \approx \frac{1}{\sqrt{\Psi_B}} \frac{\sqrt{BDp}}{\sqrt{N}} \sqrt{\frac{N\Delta}{BDp}} \\ &= \frac{\sqrt{\Delta}}{\sqrt{\Psi_B}} \approx \frac{W^{1/4}}{\sqrt{\Psi_B}} \end{aligned} \quad (29)$$

which is in agreement with the Budinger approximation.²

RESULTS

Monte Carlo Simulations

We studied a numerical phantom modelling a thorax slice. The phantom was constituted of 4 tissues (bone, fat, lung, and mediastinum) with different activities (Fig. 4, top; Table 1)

TABLE 2. Characteristics of the ROIs

Tumor ROI	Radius	Relative Uptake
ROI 1	8 pixels	6
ROI 2	6 pixels	12
ROI 3	3 pixels	20

representing the background, ie, ROI 0. We simulated three 2-ROI configurations. The ROIs stood for chest tumors with various locations, sizes, and relative uptakes with respect to the background (Fig. 3, bottom; Table 2). The object was defined and reconstructed on a 128×128 grid. Its projections were simulated using 128 projection angles over 180 degrees and 128 bins per projection angle, without taking into account the scatter or attenuation and assuming a perfect detector response. When simulating realistic noisy records, Poisson noise was added using the Knuth algorithm.³⁸ The coefficients of the radon matrix Λ were computed using a uniformly distributed pixel activity model. Two count rates were considered: 25,000 events and 400,000 events (on average). For each count rate, 250 realistic noisy replicates of the projection data were simulated and exploited to estimate the ROI parameters using different methodologies. The first evaluated methodology was the macroquantification technique. The macroprojector was computed on the basis of an image estimate produced using MLEM with iterative ROI-wise regularization. The regularization was performed by filtering the image after each iteration, ROI by ROI, with a gaussian kernel of full width at mid-height (FWMH) 1 pixel. During image reconstruction, at each iteration, the macroprojector was computed and equations (15) and (16) were used to provide an estimation of the ROI activity and variance. In what follows, the ROI estimation obtained with this technique (equation [15]) will be denoted as Macro-Q. The macroestimate of the ROI standard deviation (square root of the variance predicted using equation [16]) will be called Macro- σ . Our methodology was compared with a standard technique for ROI assessment that consists in reconstructing an estimate of the object using classical MLEM (with and without a posteriori regularization) and then summing the pixel values inside the considered ROI (equation [8]). This was done using the following parameters:

- MLEM without regularization, referred to as $MLEM_{NR}$.
- MLEM followed by postfiltering using a gaussian kernel of FWHM 1 pixel, referred to as $MLEM_{PF1}$.
- MLEM followed by postfiltering using a gaussian kernel of FWHM 2 pixels, referred to as $MLEM_{PF2}$.

The three 2-ROI configurations proposed in Figure 4 were processed separately and independently. For each configuration and each count rate, the 4 methods presented previously were run for a total of 150 iterations. During the iterative process, each of the 4 methodologies provided a set of 250 estimations of the ROI value (Macro-Q, $MLEM_{NR}$, $MLEM_{PF1}$, and $MLEM_{PF2}$) corresponding to the 250 replicates of the projection data. Furthermore, the macroquantification technique allowed the computation of 250 estimates of the ROI standard deviation (Macro- σ). Figure 5 presents the results obtained for the 3 ROI configurations after the 25,000 event simulations. The bottom curves show the evolution with the number of iterations of the mean of the 4 ROI estimators. Macro-Q is displayed using a thick line; $MLEM_{NR}$, using a thin line; $MLEM_{PF1}$, using a dashed line; and $MLEM_{PF2}$, using a dotted line. The straight gray line stands for the true ROI value. The top curves show the evolution with the iterations of the standard deviation of the 4 ROI estimators. The correspondence between the line type and the method is the same as for the bottom curves. The gray area represents the evolution with the iterations of the range ([minimum, maximum]) of the Macro- σ predictions. Figure 6 is the counterpart of Figure 5 for the 400,000 event simulations. Finally, Table 3 summarizes the quantitative results provided by the macroquantification technique for each ROI configuration and count rate. The proposed results correspond to a total of 150 iterations, when the method can be considered as having reached convergence.

TABLE 3. Monte Carlo Simulations

ROI No.	Mean Count Rate	True ROI Value	Macro-Q Mean	Relative Bias (%)	Absolute Bias	Macro-Q SD	Macro- σ (min, max)	Relative Error (%)
1	25,000	1152	1142	-0.9	-10	99	(94, 98)	(-5, -1)
	400,000	18,432	18,472	0.2	40	391	(382, 386)	(-2, -1)
2	25,000	1248	1245	-0.2	-3	98	(94, 98)	(-4, 0)
	400,000	19,968	20,193	1.1	225	390	(382, 386)	(-2, -1)
3	25,000	640	634	-0.9	-6	67	(66, 69)	(-1, 3)
	400,000	10,240	10,322	0.8	82	272	(267, 270)	(-2, -1)

Quantitative results for the macroquantification of the ROI values (values at convergence, 150 iterations).
Max indicates maximum; min, minimum.

Physical Phantom Study

The studied physical phantom was composed of a big cylinder of length $L = 54.9$ cm and diameter $B = 40.2$ cm containing 3 angularly evenly spaced small cylinders of diameter $S = 12.4$ cm located at a distance $d = 8.5$ cm from the big cylinder axis (Fig. 7). The big cylinder was filled with water. The 3 small cylinders were filled with ^{99m}Tc solutions with various activities: cylinder 1 (C_1) was filled with 1.5 mCi/L; cylinder 2 (C_2), with 1.25 mCi/L; and cylinder 3 (C_3), with 1 mCi/L. A tomographic record of the physical phantom was acquired with an Infinia Hawkeye 4 SPECT-CT dual-head gamma camera (GE Healthcare, Chalfont St Giles, United Kingdom) using the following settings: projection sampling of 128×128 corresponding to

a resolution of $4.42 \times 4.42 \text{ mm}^2$, 120 projection angles over 360 degrees, and an acquisition time of 15 seconds per projection angle. A total of 90 2-dimensional (2D) sinograms were recorded, corresponding to 90 transaxial slices of the phantom. Each 2D sinogram was corrected for Compton scattering by means of the Jaszczak method. At this point, the total number of recorded photons in the 2D sinograms exhibited a clear discordance between the internal slices and the external slices because of a significant difference in the amount of para-axial scattering affecting the internal and external slices. To produce projection data corrected for this bias, we proceeded as follows: the 90 2D sinograms were summed to create a global 120×128 2D sinogram gathering 8.12 million events (Fig. 8). This

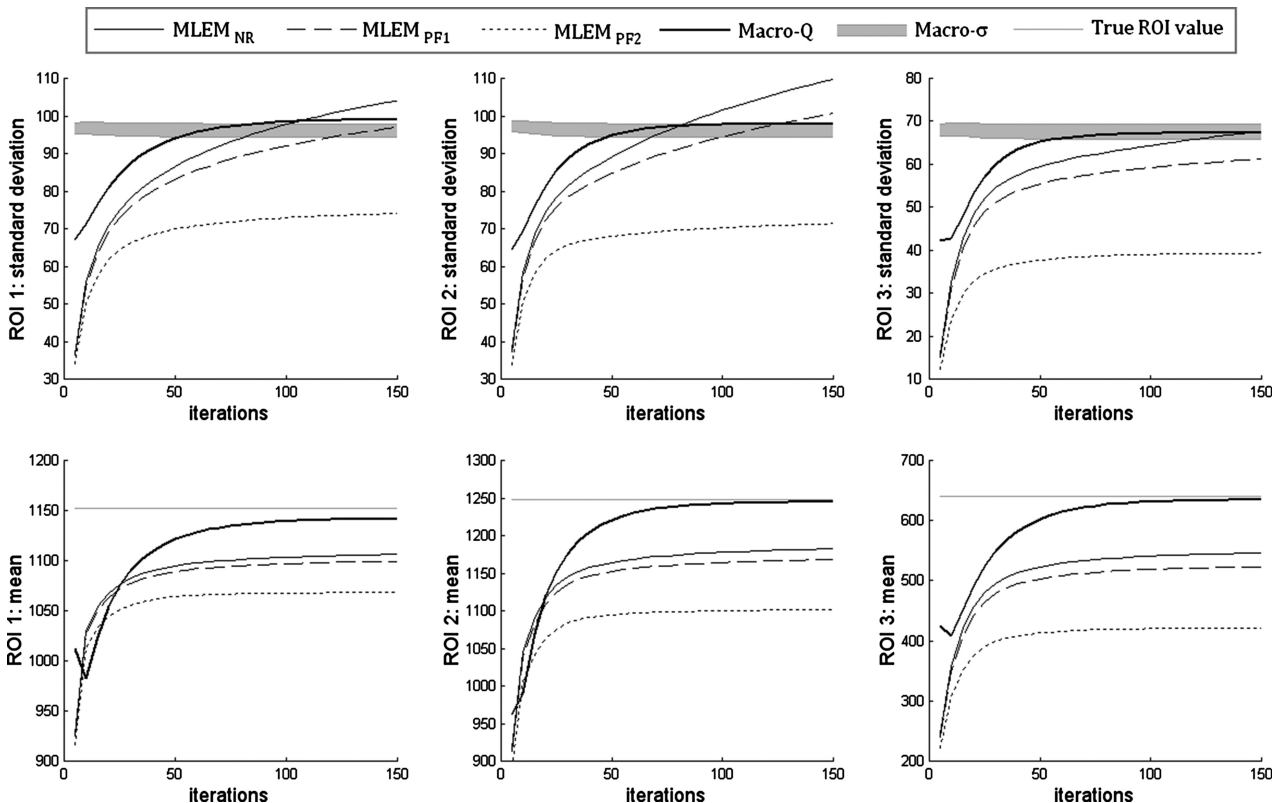


FIGURE 5. Results for the 25,000-event Monte Carlo simulations. Top, Standard deviation of the ROI value estimates along with the iterations. Bottom, Mean of the ROI value estimates along with the iterations. Left to right, ROI 1, ROI 2, and ROI 3.

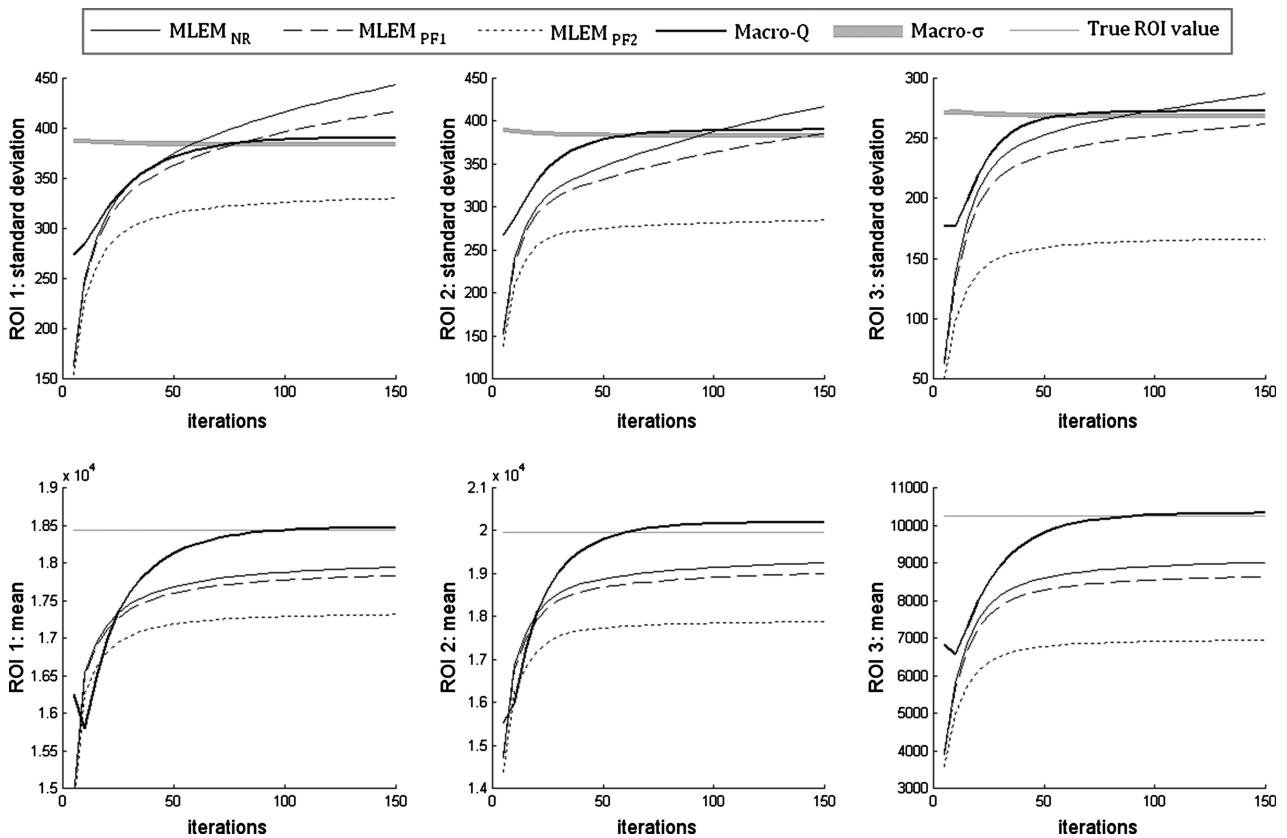


FIGURE 6. Same as Figure 4 for the 400,000-event Monte Carlo simulations.

high-statistics global sinogram was then used to generate 2 sets of low-statistics sinograms:

- The first set is constituted of 400 low-count sinograms with a mean count rate per sinogram of approximately 20,000.
- The second set is constituted of 400 high-count sinograms with an approximate mean count rate per sinogram of approximately 100,000.

A sinogram S of the first set was produced as follows: S was initialized as an identically null 120×128 matrix. Then, the global sinogram was swept through and each of the 8.12 million events had a probability $P = 1/400$ to be affected to the low-count sinogram S at the position (i, j) where it was recorded in the global sinogram. Similarly, a sinogram of the second set was produced using the same scheme with a probability $P = 1/80$. The emission images were reconstructed over a 128×128 grid. The coefficients of the system matrix were built up using the intersection area method and a uniform pixel model. The Infinia Hawkeye 4 gamma camera was coupled with a CT scanner that allowed the acquisition of a morphological density scan of the phantom. The CT reconstructed image was sampled on a $128 \times 512 \times 512$ grid. After downsampling to 128×128 to fit with the SPECT reconstruction kernel dimensions, the CT image enabled the definition of 4 ROIs (background plus 3 circular ROIs), the numbering of the ROIs corresponding to the numbering of the cylinders (Fig. 9). In addition, the CT density map allowed the correction of the system matrix components to account for autoattenuation.

We first focused on the estimation of the activity ratios between the ROIs. The ratio between ROI 1 and ROI 2

(denoted as ρ_{12}) is expected to be equal to 120%, the ratio between ROI 1 and ROI 3 (denoted as ρ_{13}) is expected to be equal to 150%, and the ratio between ROI 2 and ROI 3 (denoted as ρ_{23}) is expected to be equal to 125%. Each sinogram was evaluated in terms of these 3 ratios using the macroquantification technique. The 4 ROIs were processed all together. The macroquantification was run using a uniform macroprojector as defined in equation (20). This was legitimated by our a priori knowledge regarding the uniformity of the studied ROIs. In this case, no image needed to be reconstructed and the technique gave a punctual estimate of the following parameters:

- Region-of-interest values (Macro-Q for ROI 1, 2, and 3).
- Region-of-interest covariance matrix, from which the ROI standard deviations (Macro-σ for ROI 1, 2, and 3) are extracted.
- Region-of-interest ratios (Macro-Q for ρ_{12} , ρ_{13} , and ρ_{23}).
- Region-of-interest ratios standard deviation (Macro-σ for ρ_{12} , ρ_{13} , and ρ_{23}).

Equations (15) and (16) were used to provide an estimation of the ROI values and covariance matrix. The ROI ratios were produced by simply computing the quotient of the corresponding ROI values:

$$\text{Macro-Q}(\rho_{mn}) := \frac{\hat{\Psi}_m}{\hat{\Psi}_n} \quad (30)$$

where m and n stand for the indices of the 2 concerned ROIs. The macroestimate of the standard deviation of the ROI ratios

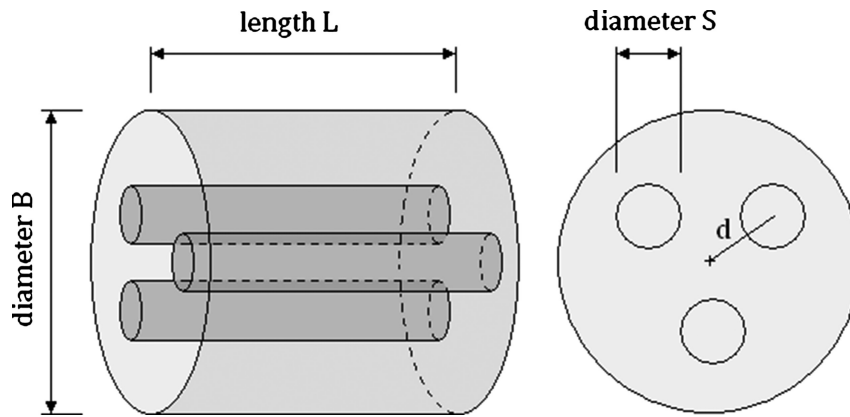


FIGURE 7. Geometry of the physical phantom: L = 59.4 cm, B = 40.2 cm, S = 12.4 cm, d = 8.5 cm.

was then computed from the ROI values and covariance matrix using the following:

$$\text{Macro_}\sigma(\rho_{mn}) = \frac{\sqrt{\hat{\Psi}_n^2 \text{Cov}_{mn}(\hat{\Psi}) + \hat{\Psi}_m^2 \text{Cov}_{mn}(\hat{\Psi}) - \hat{\Psi}_m \hat{\Psi}_n \text{Cov}_{mn}(\hat{\Psi})}}{\hat{\Psi}_n^2} \quad (31)$$

Where *m* and *n* stand for the indices of the 2 concerned ROIs. Table 4 summarizes the quantitative results provided for ROI ratio estimation.

A second series of calculations was then performed to determine to what extent the macroquantification method enabled correct comparisons between ROIs. Random pairs of sinograms were considered. Let us denote with $(\Psi_{n,1}, V_{n,1})$ and $(\Psi_{n,2}, V_{n,2})$ the corresponding pair of macroestimates of the ROI value and variance for ROI *n*. The tested null hypothesis was the following:

$$H_0 : \Psi_{n,1} = \Psi_{n,2} \Leftrightarrow \delta_n \triangleq \Psi_{n,1} - \Psi_{n,2} = 0 \quad (32)$$

The corresponding z-score was computed as follows:

$$\varepsilon_n = \frac{\Psi_{n,1} - \Psi_{n,2}}{\sqrt{V_{n,1} + V_{n,2}}} \quad (33)$$

In each sinogram set, 1000 random pairs were processed, providing 1000 samples for the distributions ε_n (*n* = 1...3). On the basis of the z-score distribution, we deduced, for each set and each ROI number, 4 statistical indicators:

- N_95: the proportion of sinogram pairs for which the 2 ROIs were considered as having equal value with a first-order risk of 5%.
- N_90: the proportion of sinogram pairs for which the 2 ROIs was considered as having equal value with a first-order risk of 10%.
- N_80: the proportion of sinogram pairs for which the 2 ROIs was considered as having equal value with a first-order risk of 20%.
- N_50: the proportion of sinogram pairs for which the 2 ROIs was considered as having equal value with a first-order risk of 50%.

Figure 10 displays the histograms of the z-scores ε_n (*n* = 1...3) for the 2 sinogram sets. For comparison, the standard normal distribution is superimposed on each subplot. Finally, Table 5 summarizes the quantitative values of the 4 aforementioned indicators for each ROI and each count rate.

DISCUSSION

Monte Carlo Simulations

First and foremost, a few points have to be highlighted regarding the validation settings. First, a thorax phantom was chosen to evaluate the methodology on a realistic working case involving a tumor ROI located inside a highly nonuniform background. The nonuniformity of the background allows evaluating the ability of the technique to produce an accurate macroprojector. Three ROI configurations were tested in the same perspective. Indeed, the macroprojector estimate has to show good accuracy whatever the ROI size, relative uptake, or location. One of the ROI configurations involves a tumor located astride 2 background structures with different activities to evaluate the behavior of the quantification technique in this



FIGURE 8. The high-statistics global 2D sinogram of the physical phantom.

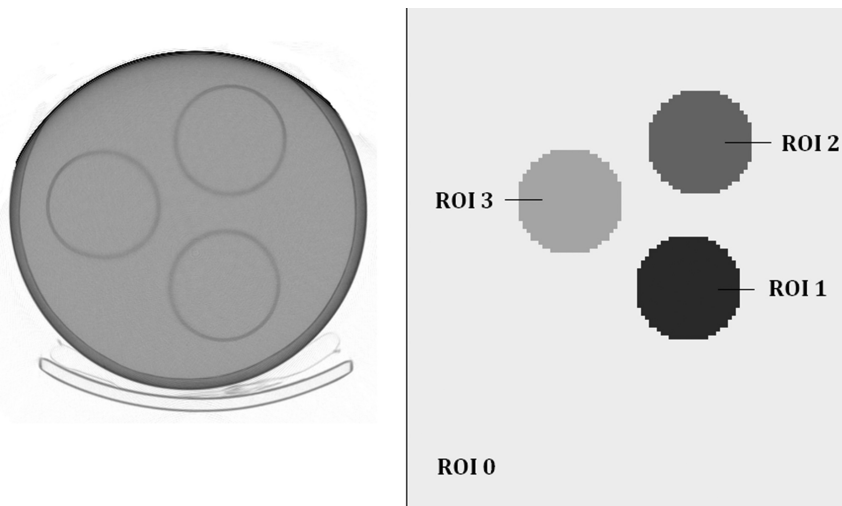


FIGURE 9. Left, Computed tomographic scan slice of the physical phantom. Right, Defined ROIs.

particularly common case. Second, it was decided not to take into account the classical measurement artifacts affecting the projections in emission tomography. All of these artifacts can be modelled inside the system matrix Λ whenever this is necessary using classical data corrections as presented elsewhere.³⁹ The imprecision affecting the system matrix components would equally affect any ROI assessment methodology by inducing a systematic bias in the ROI estimates. To judge the intrinsic qualities of macroquantification versus classical quantification methods, the same operator was used for data simulation and image reconstruction, assuming the ideal case of a perfect modeling of the system matrix. Lastly, the boundaries of the studied ROIs were considered as perfectly defined. This is justified by the fact that a CT image is increasingly available along with the SPECT or PET data allowing precise circumscription of the ROIs on a morphological basis. Moreover, the problem of ROI definition is linked to a segmentation issue beyond the scope of the present study.

The results presented in the previous section tend to be relatively homogenous, whatever the ROI configuration and count rate. Concerning classical ROI quantification using MLEM and pixel summation, Figures 5 and 6 (bottom curves) show that the ROI estimates are affected by a systematic bias caused by partial volume effects at the border of the ROI. The mean of the estimates asymptotically converges toward a limit, which always underestimates the true ROI value. As expected, this underestimation

increases when postfiltering is applied and is correlated with the width of the postfiltering kernel. Concerning the variability of the classical ROI estimates, Figures 5 and 6 (top curves) indicate that the standard deviation gradually rises with the number of iterations, without stabilizing. When strong postfiltering (MLEM_{PF2}) is applied, the variance of the estimates tends to reach a plateau but at the price of a major bias. These last considerations emphasize the difficulty to find an optimal bias/variance tradeoff using classical ROI quantification.

As for the macroquantification approach, Figures 5 and 6 demonstrate that it allows a good tradeoff between systematic bias and variance. The bottom curves show that the convergence of the mean value of Macro-Q toward the true ROI value is rather satisfying and always significantly better than with the classical method. This is supported by the quantitative results summarized in Table 3: the relative bias affecting the Macro-Q estimates never exceeds 1.1 % at convergence. This superiority of the macroscopic approach over the classical method follows from a better handling of partial volume effects at the edges of the ROI. When passing from the pixel model to the macroscopic model, the sensitivity of the system matrix to partial volume effects dramatically decreases. Regarding the variability of the Macro-Q estimates, Figures 5 and 6 (top curves) show that their standard deviation always reaches a plateau during the iterative process. Furthermore, the plateau value is fairly well approximated by the Macro- σ estimate. As shown in Table 3, the

TABLE 4. Physical Phantom Study

ROI Ratio	Mean		Macro-Q Mean	Relative Bias (%)	Absolute Bias	Macro-Q SD	Macro- σ (min, max)	Relative Error (%)
	Count Rate	True Ratio						
ρ_{12}	100,000	1.2	1.25	4.2	0.05	$11.6 \cdot 10^{-3}$	$(11.2, 12.0) \cdot 10^{-3}$	(-3, 3)
	20,000	1.2	1.25	4.2	0.05	$25.7 \cdot 10^{-3}$	$(23.9, 27.9) \cdot 10^{-3}$	(-7, 9)
ρ_{13}	100,000	1.5	1.46	-0.7%	-0.01	$14.9 \cdot 10^{-3}$	$[14.4 \ 15.6] \cdot 10^{-3}$	(-3, 5)
	20,000	1.5	1.46	0%	-0.00	$33.6 \cdot 10^{-3}$	$[31.2 \ 36.2] \cdot 10^{-3}$	(-7, 8)
ρ_{23}	100,000	1.25	1.22	-4.0%	-0.05	$13.4 \cdot 10^{-3}$	$[12.9 \ 13.9] \cdot 10^{-3}$	(-4, 4)
	20,000	1.25	1.22	-4.0%	-0.05	$30.8 \cdot 10^{-3}$	$[28.3 \ 32.9] \cdot 10^{-3}$	(-8, 7)

Quantitative results for the macroquantification of the ROI ratios.
Max indicates maximum; min, minimum.

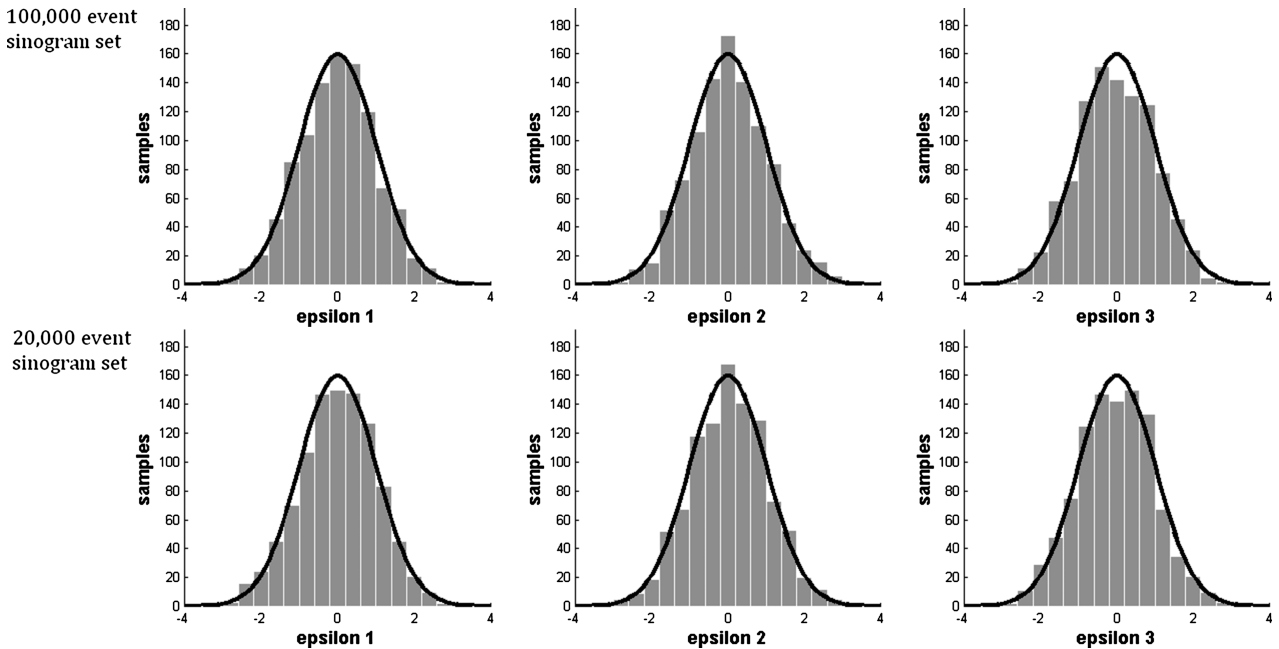


FIGURE 10. Physical phantom study. Histograms of the z-scores. Top, The 100,000-event sinogram set. Bottom, The 20,000-event sinogram set. Left to right, z-Scores ϵ_1 , ϵ_2 , and ϵ_3 . The curve of the standard normal distribution is superimposed.

Macro- σ estimates have very low dispersion with a relative error that never exceeds 5% (Macro- σ mostly underestimates the effective standard deviation). Moreover, it seems that the systematic bias is always significantly lower than the standard deviation is, which means that the unknown error (ie, the bias) remains small compared with the controlled error (ie, the statistical uncertainty fairly well approximated with Macro- σ).

Physical Phantom Study

The physical phantom study evaluated the macroquantification technique in the frame of ROI comparison. The a priori assumption regarding the uniformity of the ROIs allowed exploiting the simple formulation on the basis of the uniform macroprojector. A first series of calculations tested the ability of the method to estimate the expectation and variance of the activity ratio between 2 ROIs. The results shown in Table 4 demonstrate the good ability of macroquantification to recover the exact values of the ROI ratios, with a relative bias always lower than 5%. The observed bias is likely caused by a resolution loss induced by the extraction of the ROI boundaries on a 128×128 kernel using the 512×512 CT image. Concerning the dispersion indicators, Table 4 shows a very good agreement between the Macro-Q standard deviations and the Macro- σ predictions: the relative error ranges from -4% to 5% for the 100,000-event sinogram set and from -8% to 9% for the 20,000 event sinogram set.

A second series of calculations was performed to assess the efficiency of macroquantification in ROI comparison. A statistical test was applied to pairs of ROIs having theoretically equal activity levels. Figure 10 shows that the computed z-score histograms perfectly fit with the expected standard normal distribution. Accordingly, the statistical indicators presented in Table 5 show perfect agreement with the expected values of 95%, 90%, 80%, and 50%, whatever the studied ROI and count rate. The physical phantom study thereby confirms the ability of macroquantification to provide robust and accurate estimates of

ROI statistical parameters in realistic working conditions (approximate knowledge of the system matrix and a posteriori circumscription of the ROIs using morphological information). Whenever this is necessary for clinical decision, the accuracy of the Macro- σ predictions is broadly sufficient to provide a helpful insight into the order of magnitude of the ROI (or ROI ratio) variance. As discussed, the quality of the variance estimate allows for efficient comparisons between ROIs using classical statistical tests. When the studied ROIs are a priori known to be homogenous, which is current in routine practice (striatal neurodopaminergic imaging, for instance⁴⁰), the use of the uniform macroprojector enables an extremely fast computation of the ROI parameters (less than 1 second on a personal computer) without involving any image reconstruction. This should be particularly helpful in the frame of dynamic imaging implying ROI quantification together with low-statistics data and stringent time-management constraints.

CONCLUSIONS

In this article, we described an innovative methodology for the statistical characterization of ROIs. The cornerstone of the technique is the rearrangement of the projection data into

TABLE 5. Physical Phantom Study

ROI	Count Rate	N_95	N_90	N_80	N_50
1	100,000	94.3%	89.1%	80.3%	49.7%
	20,000	94.6%	89.1%	78.1%	50.7%
2	100,000	94.6%	90.1%	78.2%	48.1%
	20,000	94.0%	90.1%	79.5%	50.4%
3	100,000	95.1%	89.5%	80.5%	49.5%
	20,000	95.7%	89.9%	78.9%	47.7%

Statistical indicators for ROI comparison.

macroprojections that are linked to the ROI activities through a macroprojector. We proposed a strategy for the computation of the macroprojector using iterative image reconstruction coupled with ROI-wise smoothing. We first evaluated the results of the methodology through Monte Carlo simulations on the basis of a thorax phantom and involving various tumor ROI configurations and count rates compatible with clinical practice. For the sake of convenience and to judge the intrinsic ability of the method to quantify ROI activities, the measurement artifacts affecting the projection data was neglected and a perfect a priori definition of the ROIs was considered. The results indicated that macroquantification allows an optimal handling of the ROI statistical parameters. The provided ROI estimations significantly reduced the systematic bias compared with classical ROI assessment, and the variance estimation produced by the macroscopic approach fairly well agreed with the effective variance of the macroscopic ROI estimates. Next, we validated the new methodology using SPECT data of a physical phantom. The task was to compare 3 ROIs defined on the basis of a coregistered CT image. Here again, the bias affecting the ROI ratio estimates was almost negligible and always less than 5% of the true ROI ratio. The ratio variance estimates targeted fairly well the order of magnitude of the measured variances, with a maximum relative error ranging from approximately 5% for the high-count sinograms to approximately 10% for the low-count ones. The quality of these variance estimations allowed highly accurate ROI comparisons using standard statistical decision tests. Owing to its intrinsic simplicity, the macroquantification approach allows fast computations compatible with a wide range of routine clinical applications.

REFERENCES

- Huesman RH. Effects of a finite number of projection angles and finite lateral sampling of projections on the propagation of statistical errors in transverse section reconstruction. *Phys Med Biol.* 1977;22:511–521.
- Budinger TF, Derenzo SE, Gullberg GT, et al. Emission computer assisted tomography with single-photon and positron annihilation photon emitters. *J Comput Assist Tomogr.* 1977;1:131–145.
- Alpert NM, Chesler DA, Correia JA, et al. Estimation of the local statistical noise in emission computed tomography. *IEEE Trans Med Imaging.* 1982;1:142–146.
- Snyder DL, Miller MI, Thomas LJ, et al. Noise and edge artifacts in maximum-likelihood reconstructions for emission tomography. *IEEE Trans Med Imaging.* 1987;6:228–238.
- Moore SC, Kijewski MF, Müller SP, et al. SPECT image noise power: effects of nonstationary projection noise and attenuation compensation. *J Nucl Med.* 1988;29:1704–1709.
- Gillen GJ. A simple method for the measurement of local statistical noise levels in SPECT. *Phys Med Biol.* 1992;37:1573.
- Tapiovaara MJ, Wagner RF. SNR and noise measurement for medical imaging: I. A practical approach based on statistical decision theory. *Phys Med Biol.* 1993;38:71–92.
- Tapiovaara MJ. SNR and noise measurement for medical imaging: II. Application to fluoroscopic x-ray equipment. *Phys Med Biol.* 1993;38:1761–1788.
- Wilson DW, Tsui BW. Noise properties of filtered-backprojection and ML-EM reconstructed emission tomography images. *IEEE Trans Nucl Sc.* 1993;40:1198–1203.
- Liew SC, Hasegawat BH, Brown JK, et al. Noise propagation in SPECT images reconstructed using an iterative maximum-likelihood algorithm. *Phys Med Biol.* 1993;38:1713–1726.
- Kim HJ, Zeeberg BR, Reba RC. Evaluation of reconstruction algorithms in SPECT neuroimaging: I. Comparison of statistical noise in SPECT neuroimages with “naive” and “realistic” predictions. *Phys Med Biol.* 1993;38:863–873.
- Kim HJ, Zeeberg BR, Reba RC. Evaluation of reconstruction algorithms in SPECT neuroimaging: II. Computation of deterministic and statistical error components. *Phys Med Biol.* 1993;38:881–895.
- Barrett HH, Wilson DW, Tsui BM. Noise properties of the EM Algorithm: I. Theory. *Phys Med Biol.* 1994;39:833–846.
- Barrett HH, Wilson DW, Tsui BM. Noise properties of the EM algorithm: II. Monte Carlo simulations. *Phys Med Biol.* 1994;39:847–872.
- Pan X, Metz CE. Analysis of noise properties of a class of exact methods of inverting the 2-D exponential radon transform. *IEEE Trans Med Imaging.* 1995;14:4:659–668.
- Wang W, Gindi G. Noise analysis of MAP-EM algorithms for emission tomography. *Phys Med Biol.* 1997;42:2215–2232.
- Kadmas DJ, DiBella EVR, Huesman RH, et al. Analytical propagation of errors in dynamic SPECT: estimators, degrading factors, bias and noise. *Phys Med Biol.* 1999;44:1997–2014.
- Jinyi Q, Leahy RM. Fast computation of the covariance of MAP reconstructions of PET images. *SPIE Proceedings Series.* 1999;3661:344–355.
- Nuyts J. On estimating the variance of smoothed MLEM images. *IEEE Trans Nucl Sc.* 2002;40:714–721.
- Mariano-Goulart D, Fourcade M, Bernon JL, et al. Experimental study of stochastic noise propagation in SPECT images reconstructed using the conjugate gradient algorithm. *Comp Med Imaging Graph.* 2003;27:53–63.
- Nickerson LD, Narayana S, Lancaster L, et al. Estimation of the local statistical noise in positron emission tomography revisited: practical implementation. *Neuroimage.* 2003;19:442–456.
- Fessler JA. Mean and variance of implicitly defined biased estimators (such as penalized maximum likelihood): applications to tomography. *IEEE Trans Image Proc.* 1996;5:493–506.
- Haynor DR, Woods SD. Resampling estimates of precision in emission tomography. *IEEE Trans Med Imaging.* 1989;8:337–343.
- Buvat I. A bootstrap approach for analyzing the statistical properties of SPECT and PET images. *Phys Med Biol.* 2002;47:1761–1775.
- Rico A, Strauss O, Mariano-Goulart D. Choquet integrals as projection operators for quantified tomographic reconstruction. *Fuzzy Sets and Systems.* 2009;160:198–211.
- Strauss O, Lahrech A, Rico A, et al. NIBART: a new interval based algebraic reconstruction technique for error quantification of emission tomography images. *Med Image Comput Comput Assist Interv.* 2009;12:148–155.
- Huesman RH. A new fast algorithm for the evaluation of regions of interest and statistical uncertainty in computed tomography. *Phys Med Biol.* 1984;29:543.
- Carson RE. A maximum likelihood method for region-of-interest evaluation in emission tomography. *J Comput Assist Tomogr.* 1986;10:654–663.
- Formiconi AR. Least squares algorithm for region-of-interest evaluation in emission tomography. *IEEE Trans Med Imaging.* 1993;12:90–100.
- Carson RE, Yan Y, Daube-Witherspoon ME, et al. An approximation formula for the variance of PET region-of-interest values. *IEEE Trans Med Imaging.* 1993;12:240–250.
- Vanzi E, De Cristofaro MT, Ramat S, et al. A direct ROI quantification method for inherent PVE correction: accuracy assessment in striatal

- SPECT measurements. *Eur J Nucl Med Mol Imaging*. 2007; 34:1480–1489.
32. Dempster AP, Laird NM, Rubin DB. Maximum likelihood from incomplete data via the EM algorithm. *J Royal Stat Soc B*. 1977;38:11–38.
 33. Shepp LA, Vardi Y. Maximum likelihood reconstruction for emission tomography. *IEEE Trans Med Imaging*. 1982;1:113–122.
 34. Cloquet C. MLEM and OSEM deviate from the Cramer-Rao bound at low counts. *IEEE Trans Nucl Sc*. 2013;60–1:134–143.
 35. Slijpen ETP, Beekman FJ. Comparison of post-filtering and filtering between iterations for SPECT reconstruction. *IEEE Trans Nucl Sci*. 1999;46:2233–2238.
 36. Silverman BW, Jones MC, Wilson JD, et al. A smoothed EM approach to indirect estimation problems, with particular reference to stereology and emission tomography. *J R Statist Soc B*. 1990;52:271–324.
 37. Mustafovic S, Thielemans K, Hogg D, et al. Object dependency of resolution and convergence rate in OSEM with filtering. *IEEE Nucl Sci Symp Conference Rec*. 2001;3:1786–1790.
 38. Knuth DE. *Seminumerical Algorithms. The Art of Computer Programming*, Vol 2. Addison Wesley, Boston; 1969.
 39. Zaidi H. *Quantitative Analysis in Nuclear Medicine Imaging*. New York, NY: Springer-Verlag; 2006.
 40. Soret M, Koulibaly PM, Darcourt J, et al. Quantitative accuracy of dopaminergic neurotransmission imaging with ^{123}I SPECT. *J Nucl Med*. 2003;44:1184–1193.